


**Ultrafast carrier and lattice dynamics in the Dirac semimetal NiTe<sub>2</sub>**L. Cheng<sup>1</sup>, F. C. Fei<sup>2</sup>, H. Hu<sup>1</sup>, Y. M. Dai<sup>2</sup>, F. Q. Song<sup>2</sup>, and J. Qi<sup>1,\*</sup><sup>1</sup>*State Key Laboratory of Electronic Thin Films and Integrated Devices, University of Electronic Science and Technology of China, Chengdu 610054, China*<sup>2</sup>*College of Physics, Nanjing University, Nanjing 210093, China* (Received 25 April 2022; accepted 23 August 2022; published 26 September 2022)

Here, using the ultrafast optical pump-probe spectroscopy, we have studied the quasiparticle dynamics in the type-II Dirac semimetal NiTe<sub>2</sub>. Anomalous dynamic optical responses are detected around a critical temperature  $T^*$  ( $\sim 60$  K), which is also evidenced by the transport experiment. In specific, our results reveal a phonon-assisted electron-hole recombination process showing an anomaly at  $T^* \simeq 60$  K. We discover an unusual phonon renormalization behavior, manifested by the  $T$ -dependent phonon energy and lifetime exhibiting anomalies at  $T^*$ . We unveil that the observed anomalous  $T$ -dependencies can be attributed to the sudden shift of the phonon mode involved in the recombination, which originates from the abrupt change of electronic structure near the Fermi surface. These findings can provide deeper insight into the nonequilibrium carrier and lattice properties in the topological materials.

DOI: [10.1103/PhysRevB.106.104308](https://doi.org/10.1103/PhysRevB.106.104308)**I. INTRODUCTION**

The electronic structure near the Fermi surface plays a vital role in the equilibrium and quasiequilibrium properties of the condensed-matter systems [1–4], which may have complex Fermi surface topology that is essential to the emergent phenomena in the transport and optical experiments [5–7]. In particular, the quasiparticle relaxation via the scattering processes necessitates clarification during the evolution of the Fermi surfaces. The related physics is intricate since it involves the nonequilibrium fermionic quasiparticles and bosonic excitations interacting with each other, i.e., electrons and holes for the former, and phonons and other low-energy collective modes for the latter. So far, it is still not fully understood how the dynamics of fermionic quasiparticle in different materials responds to the bosonic modes upon the sudden variation of the electronic structure in  $k$ -space, although the related information can be essential to understand the experimental results and can be useful for developing future electronic and optoelectronic devices.

In the past years, topological semimetals (TSMs) have attracted significant interest in the condensed-matter and material physics [8–11] due to many exotic properties induced by their unique Fermi surface topology. Typical TSMs, such as the Dirac semimetal, the Weyl semimetal, and the nodal-line semimetal, have conical dispersion and belong to the so-called type-I TSMs. There exists another type of quantum matter called type-II TSMs [12,13], which are characterized by strongly tilted Dirac cones. Consequently, the associated band topology in type-II TSMs leads to a variety of interesting phenomena, e.g., the direction-dependent chiral anomaly, unusual superconductivity, exotic quantum oscillations, and

giant nonlinear optical responses [14–17]. Clearly, the type-II TSMs provide nice testbeds for studying the dynamic properties of the fermionic quasiparticles and collective excitations.

Very recently, among the type-II TSMs, the Ni-based compound NiTe<sub>2</sub> was proposed to host the Dirac fermions in the vicinity of the Fermi energy (tens of meV above  $E_f$ ) [18]. Many experimental studies on NiTe<sub>2</sub> [18–25] have been carried out and primarily focus on investigating the transport properties [21–23] that are potentially associated with the topological band structure of this material. Here, using the ultrafast optical pump-probe spectroscopy [see Fig. 1(a)], we reveal the dynamic properties of nonequilibrium carriers and phonons, which are critical to the electrical transport in the single crystal NiTe<sub>2</sub>. Our measurements reveal a peculiar temperature-dependent phonon-assisted recombination process whose decay manifests an anomaly near  $T^* \simeq 60$  K. Moreover, we identify a coherent phonon mode whose temperature evolution of energy and lifetime can greatly deviate from that of the conventional anharmonic phonon-decay model and, particularly, shows unusual behaviors across  $T^*$ . Detailed analysis shows that these abnormal phenomena can be attributed to the sudden electronic structure change near the Fermi surface as the temperature crosses  $T^*$ , or to the eminent Lifshitz transition [26]. These results present us critical information for understanding and controlling the nonequilibrium or quasiequilibrium properties of the topological materials and other similar systems.

**II. EXPERIMENT AND RESULTS**

The NiTe<sub>2</sub> sample in our experiments is a single crystal,  $\sim 1$  mm in size, which was grown by the self-flux method [21]. During the sample growth, the mixture of nickel powder (99.9%) and tellurium shot (99.99%) with a molar ratio of 1:15 was prepared and sealed in an evacuated quartz tube.

\*jbqi@uestc.edu.cn

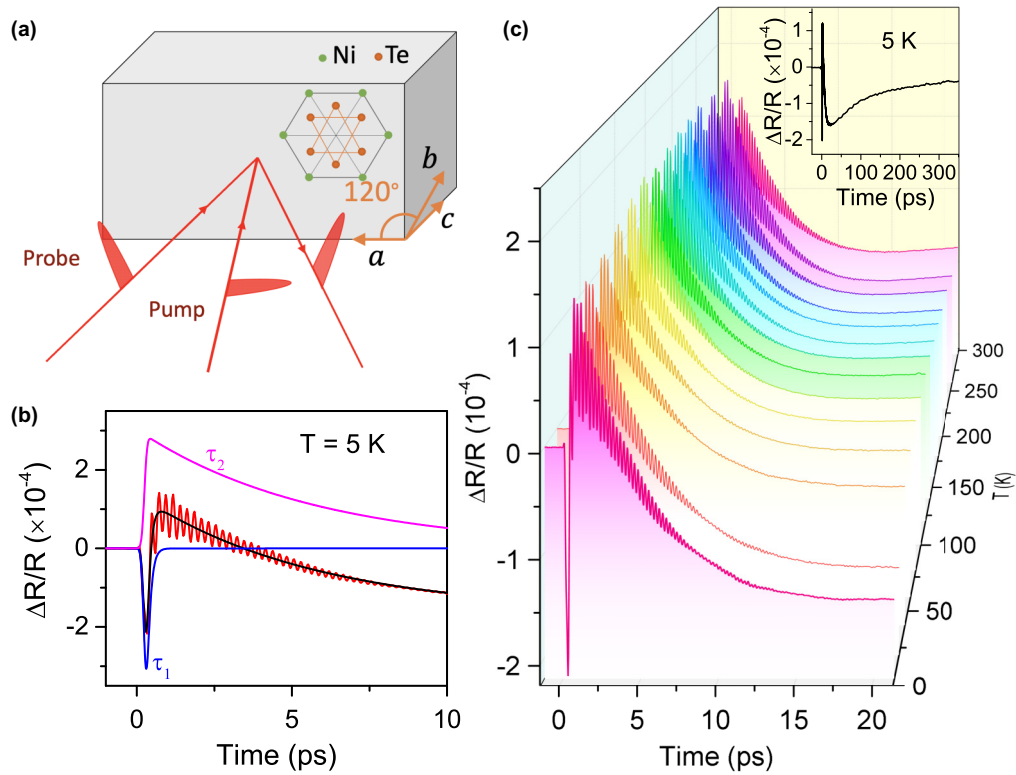


FIG. 1. (a) Schematic of experimental setup. (b) The transient reflectivity  $\Delta R(t)/R$  (red line) as a function of time delay in NiTe<sub>2</sub> at  $T = 5$  K and  $F = 1.6 \mu\text{J}/\text{cm}^2$ . The black solid line shows the fit to the measured data, without including the oscillations. The magenta and the blue curves represent the contributions of fast and slow relaxation processes obtained from the fitting. (c)  $\Delta R(t)/R$  as a function of time at selected temperatures. The inset in panel (c) shows the  $\Delta R(t)/R$  signal up to 350 ps.

Then the tube was heated to 700 °C for 12 h, and gradually cooled down to 500 °C within a week. The prepared sample was characterized by x-ray diffraction and scanning electron microscopy, respectively, and the results show its high quality. The details of sample characterization are shown in Appendix A.

In our work, the transient reflectivity of NiTe<sub>2</sub> was measured at a center wavelength of 800 nm ( $\sim 1.55$  eV) using a Ti:sapphire femtosecond laser with a pulse width of  $\sim 55$  fs (full width at half maximum), whose repetition rate was 80 MHz. During the measurements, the typical pump fluence was  $1.6 \mu\text{J}/\text{cm}^2$ , and the power ratio between pump and probe was 10:1. The sample was mounted in a cryostat whose temperature could be controlled from 5 to 300 K with an accuracy of  $\sim 0.1$  K. More information about the experimental setup can also be found in Refs. [27–30].

Figure 1(c) shows the typical transient reflectivity  $\Delta R(t)/R$  signals measured from  $\sim 5$  K to room temperature. Initially, photoexcitation results in a sharp drop in  $\Delta R(t)/R$  due to the thermalization of the electronic system via the electron-electron ( $e-e$ ) scattering. Thereafter, a fast recovery of the photoinduced reflectivity change occurs within  $\sim 300$  fs, after which there exists a relatively slow decay process followed by a very slow recovery extending to several hundreds of picoseconds. In addition, the  $\Delta R(t)/R$  signals also display clear damped oscillations superimposed on the nonoscillating background. Here, we discuss the decaying and oscillating components in succession.

### A. Ultrafast decay processes

We first focus on the nonoscillatory signals within  $\sim 20$  ps, i.e., the two relaxation components mentioned above. The very slow recovery dynamics is not discussed since it is mainly due to the thermal diffusion process. In order to quantitatively extract the relaxation time, the measured  $\Delta R(t)/R$  signal before  $\sim 20$  ps is fitted using the following formula [29,31],

$$\frac{\Delta R(t)}{R} = \left( \sum_{j=1,2} A_j e^{-\frac{t}{\tau_j}} + C \right) \otimes G(t), \quad (1)$$

where  $A_j$  and  $\tau_j$  ( $j = 1$  and  $2$ ) are the amplitudes and decay times of the two relaxation processes, respectively.  $C$  is a constant representing the long recovery process that is beyond our research interest (much longer than 20 ps), and  $G(t)$  is a Gaussian function standing for the pump-probe cross correlation. As seen in Fig. 1(b), the fitted curve is in excellent agreement with the nonoscillating part of the experimental data. And we found that  $A_1 < 0$  and  $A_2 > 0$  for all the temperatures, while  $\tau_1$  and  $\tau_2$  characterizing the lifetimes of fast and slower relaxation processes are strongly temperature dependent. In order to gain insight into the origin of the two relaxation processes, a careful examination of the temperature-dependent relaxation dynamics is indispensable. The extracted  $\tau_1$  and  $\tau_2$  values as a function of temperature are shown in Figs. 2(a) and 2(b).

In general, after the  $e-e$  thermalization, the hot carriers start to transfer their excess energy to the lattice system with

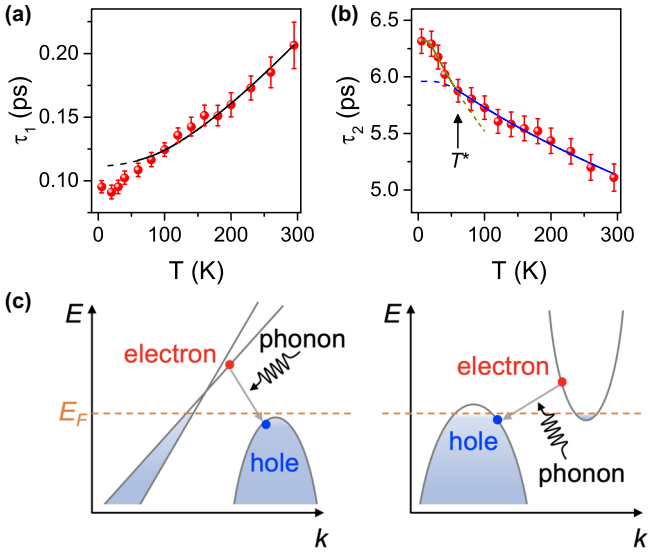


FIG. 2. Panels (a) and (b) show  $\tau_1$  and  $\tau_2$ , respectively, as a function of temperature for pump fluence of  $\sim 1.6 \mu\text{J}/\text{cm}^2$ . The curves denote (a) the TTM fit (black solid curve) and (b) the calculated temperature dependence of the phonon-assisted  $e$ - $h$  recombination time (the dark yellow and the blue curves are the fittings with different temperature ranges). (c) Schematic of the potential hot-carrier cooling processes via the phonon-assisted electron-hole recombination in  $\text{NiTe}_2$ .

a sub-picosecond timescale via the electron-phonon ( $e$ - $ph$ ) scattering in metals and semimetals [32–34]. Therefore, considering  $\tau_1$  with a timescale of  $\sim 100$  fs, we can reasonably attribute its associated decay process to the  $e$ - $ph$  scattering, which, in principle, can be described by the two-temperature model (TTM). Figure 2(a) shows the result obtained by the TTM (see fitting details in Appendix B). We notice that  $\tau_1$  above  $\sim 80$  K can be fitted well using the TTM. There exists a clear discrepancy between the fitted curve and the experimental data at  $T < 80$  K, and it can be ascribed to the invalidity of the TTM at low temperatures. This is because the TTM is only applicable for the systems with well-defined temperatures, i.e., the  $e$ - $e$  thermalization time should be shorter than the  $e$ - $ph$  scattering time, which, however, is not always true, especially at low temperatures ( $T < \Theta_D/5$ ) [34–36]. This is consistent with our observation in  $\text{NiTe}_2$ , which has a fitted Debye temperature of  $\Theta_D \simeq 340$  K. Employing  $\tau^{-1} = 3\hbar\lambda\langle\omega^2\rangle(\pi k_B T_e)^{-1}$ , we can further obtain the dimensionless  $e$ - $ph$  coupling constant  $\lambda$  to be  $\sim 0.69$ , which has the same order with the values obtained in the other topological materials [37,38]. In fact, we also obtained the value of  $\tau_1$  as a function of pump fluence, which is consistent with the TTM as shown in Fig. 6 in Appendix C, confirming that the TTM is able to explain the fast relaxation process in our observations.

Differing from the fast relaxation characterized by  $\tau_1$ , the  $\tau_2$ -decay process cannot be attributed to the  $e$ - $ph$  scattering since its temperature dependence is clearly opposite to that of  $\tau_1$ , as seen in Figs. 2(a) and 2(b). One may consider first the radiative recombination across a direct gap, which, however, can be excluded since such a process usually takes a timescale of a few nanoseconds [39]. Based on the electronic structure

of  $\text{NiTe}_2$  [18,20,40], two unique properties can be found: (i) it has strongly tilted Dirac cones near the valence band maxima, and (ii) there exist the conduction and valence band extrema in close proximity within the Brillouin zone. Since the nonequilibrium electrons (holes) can still accumulate in the conduction (valence) bands after the  $e$ - $ph$  thermalization process, these two properties may facilitate the phonon-involved electron-hole ( $e$ - $h$ ) creation and recombination processes [41]. In particular, the phonon-assisted  $e$ - $h$  recombination has already been observed via the quasiparticle decay in several topological materials [42–45], where the timescale and the temperature dependence are nearly the same as those of  $\tau_2(T)$  observed here. Therefore, we attribute the  $\tau_2$  process to this type of recombination, which can be quantitatively described by [42–44]

$$\frac{1}{\tau_2} = A \frac{x}{\sinh^2 x} + \frac{1}{\tau_0}, \quad (2)$$

where  $x = \hbar\omega_r/2k_B T$ , and  $\omega_r$  corresponds to the frequency of the phonon mode involved in the  $e$ - $h$  recombination.  $\tau_0$ , a temperature-independent parameter, represents the indirect recombination process which relies on the impurities or defects of the sample.  $A$  is a parameter related to not only the density of states (DOS) in the conduction and valence bands but also to the matrix elements of the  $e$ - $h$  scattering via the  $e$ - $ph$  coupling. Figure 2(b) demonstrates that the fitted results are in excellent agreement with the experimental data, strongly supporting that the decay process characterized by  $\tau_2$  originating from the phonon-assisted  $e$ - $h$  recombination. However, in order to get a best fit, we found that the values of  $\omega_r$  and  $\tau_0$  both experience sudden variation as  $T$  crosses a critical temperature  $T^*$  ( $\sim 60$  K), i.e.,  $\omega_r/2\pi \simeq 1.6$  THz and  $\tau_0 \simeq 6.3$  ps for  $T < T^*$  while  $\omega_r/2\pi \simeq 4.3$  THz and  $\tau_0 \simeq 5.9$  ps for  $T > T^*$ . Since (i) both the energy and the momentum are conserved during the indirect recombination and (ii) the impurity or defect level relative to the electron and hole bands (or pockets) influences the recombination time, the sudden variation of  $\omega_r$  and  $\tau_0$  suggests that near  $E_F$  there emerges an abrupt change of the electronic structures associated with the electron and hole pockets.

Note that a similar decay process was also observed in the Weyl semimetal  $\text{WTe}_2$  [44]. However,  $\tau_2$  in our sample is less temperature dependent at  $T > T^*$ , which is due to the relatively smaller parameter  $A$  in Eq. (2). This could be explained by the difference of electronic structures between  $\text{NiTe}_2$  and  $\text{WTe}_2$ , where there exist the distinct DOS and scattering matrix elements. Additionally, in the low-temperature regime, the lifetime of the slow relaxation process in  $\text{WTe}_2$  decreases with  $T$  decreasing. This is attributed to two factors: (i) the expansion of the hole pocket at lower temperatures and (ii) the temperature-dependence of interband  $e$ - $ph$  scattering [44]. Clearly, we observed an opposite temperature dependence of  $\tau_2$  at  $T < T^*$  in  $\text{NiTe}_2$ . Considering that the trend of  $\tau_2$  still obeys the phonon-assisted recombination model at  $T < T^*$ , we believe that the two factors mentioned above play a minor role in our observation, and, by contrast, the conventional phonon-assisted recombination model can still be applied in our case. The different temperature-dependent behaviors of  $\text{WTe}_2$  and  $\text{NiTe}_2$  at  $T < T^*$  should be related to their different

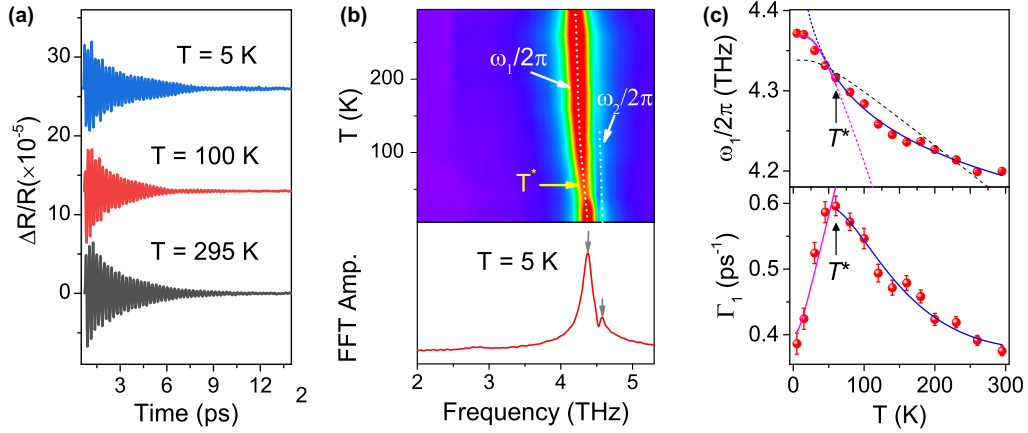


FIG. 3. (a) Extracted oscillations for three typical temperatures: 5, 100, and 295 K. (b) The Fourier-transformed spectra as a function of temperature in the frequency domain. (c) Frequency and damping rate of the phonon mode  $\omega_1$ , which are determined via Eq. (3). The magenta and the blue solid curves represent the fits using different models at  $T < T^*$  and  $T > T^*$ , respectively. The black dashed curve represents the fit using the anharmonic phonon model within the full temperature range.

electronic structures and needs to be further studied in the future.

### B. Ultrafast coherent phonons

We now focus on the oscillatory part of  $\Delta R/R$ . The oscillation signals with terahertz (THz) frequency in the transient reflectivity usually arise from the coherent optical phonons, which are initiated either via the displacive excitations or the coherent Raman process [46,47]. Figure 3(a) shows several typical time-domain oscillations, while the temperature-dependent frequency-domain data are shown in Fig. 3(b). It is obvious that the mode with a frequency of  $\sim 4.3$  THz ( $\omega_1/2\pi$ ) persists up to the room temperature. According to the previous Raman spectroscopy study on NiTe<sub>2</sub> [40], this mode should belong to the  $A_{1g}$  optical phonon mode. Another oscillatory component with a frequency of  $\sim 4.5$  THz ( $\omega_2/2\pi$ ) gradually diminishes as the temperature increases, and its temperature-dependent frequency response is also consistent with the anharmonic phonon model described below (the details are in Appendix D). In this work, we mainly discuss the  $\omega_1$  mode. In order to quantitatively explore the properties of the coherent phonon mode, we use the following equation to fit the time-domain oscillatory signals:

$$[\Delta R(t)/R]_{\text{osc}} = \sum_{j=1,2} A_j e^{-\Gamma_j t} \sin(\omega_j t + \phi_j), \quad (3)$$

where  $A_j$ ,  $\Gamma_j$ ,  $\omega_j$ , and  $\phi_j$  ( $j = 1$  and  $2$ ) are the amplitude, damping rate, frequency, and phase of the two modes, respectively. The fitted key parameters  $\omega_j/2\pi$  and  $\Gamma_j$  are listed in the Fig. 3(c) ( $j = 1$ ) and Appendix B ( $j = 2$ ). We note that in the Fourier-transformed spectra, there also exists a phonon mode around 2.7 THz [40], which is due to the  $E_g$  phonon mode and strongly depends on the pump polarization (see Appendix C for details). The configuration used here safely guarantees this mode is nearly unnoticeable and hence will not complicate the extraction of the values of  $\omega_1$  and  $\omega_2$  from the time-domain signals.

The temperature-dependent renormalizations of the phonon energies and decay rates generally are determined by

the anharmonic phonon-decay process [48–50] and are given by

$$\omega^{\text{ph-ph}}(T) = \omega_0 + a_1 \left[ 1 + 2n_B\left(\frac{\omega_0}{2}, T\right) \right], \quad (4)$$

$$\Gamma^{\text{ph-ph}}(T) = \Gamma_0 + a_2 \left[ 1 + 2n_B\left(\frac{\omega_0}{2}, T\right) \right]. \quad (5)$$

Here,  $\omega_0$  and  $\Gamma_0$  are the intrinsic frequency and the damping rate, respectively.  $a_j$  and  $b_j$  ( $j = 1$  and  $2$ ) are the fitting parameters.  $n_B(\omega, T) = [e^{\hbar\omega/k_B T} - 1]^{-1}$  is the Bose-Einstein distribution function. Usually, in the anharmonic phonon model,  $\Gamma$  increases with increasing temperature, while  $\omega$  shows the opposite  $T$  dependence. However, as shown in Fig. 3(c), the temperature-dependent fitted parameters ( $\Gamma_1$  and  $\omega_1$ ) for the  $\omega_1$  mode manifest in more complicated trends, which are beyond the anharmonic phonon model. Specifically, as the temperature increases, (i)  $\Gamma_1$  enhances quickly until the temperature reaches  $\sim 60$  K and then shows a continuous decrease; and (ii) the frequency of  $\omega_1$  mode, starting from a saturate value, experiences a relative quick drop before  $\sim 60$  K and then decreases slowly. To our knowledge, such exotic temperature-dependent renormalization of the coherent phonon properties are rarely seen in the experiments.

When examining the  $\omega_1$  phonon mode, surprisingly, we found its energy coincides well with that of the phonon involving the  $e$ - $h$  recombination at  $T > T^*$  discussed above. Besides, the anomalous temperature of  $\sim 60$  K observed in  $\Gamma_1(T)$  and  $\omega_1(T)$  is also the same as the critical temperature  $T^*$  observed in  $\tau_2(T)$ . Evidently, these results strongly suggest that the exotic  $T$ -dependent behaviors of  $\Gamma_1$  and  $\omega_1$  may emerge when the  $\omega_1$  mode starts to participate in the phonon-assisted  $e$ - $h$  recombination process, i.e.,  $\omega_1 \sim \omega_r$  at  $T \geq T^*$ . Alternatively, the unusual renormalization behavior should be related to the abrupt change of the electronic structures around  $T^*$ . In principle, the  $T$ -dependent phonon renormalization includes two contributions: depopulation and decoherence [51]. The former, often referred to as the anharmonic phonon effect, dominates in general. The latter may play a role if the strong  $e$ - $ph$  coupling and/or non-negligible defects exist in the studied material. Obviously, at  $T \geq T^*$ ,

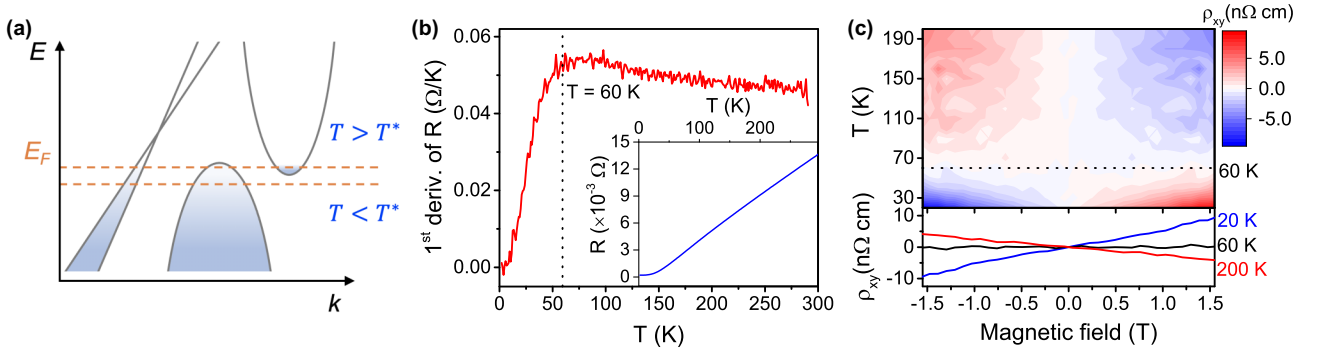


FIG. 4. (a) The schematic of the Lifshitz transition in NiTe<sub>2</sub>. (b) The first derivative of the  $T$ -dependent resistance, which clearly shows the change near 60 K. The inset is the resistance of NiTe<sub>2</sub> as a function of temperature. (c) The Hall resistivity ( $\rho_{xy}$ ) as a function of the magnetic field at different temperatures, where the sign flip of its slope appears at  $T \sim 60$  K.

the phonon-assisted  $e$ - $h$  recombination involving the  $\omega_1$  mode will trigger the decoherence effect due to the  $e$ - $ph$  interaction playing the key role in such a process and hence leads to the  $T$ -dependent damping rate  $\Gamma_{e-ph}$ , which can be described as [45,52]

$$\Gamma^{e-ph}(T) = \Gamma_0^{e-ph} \left[ f\left(-\frac{\omega_0}{2}, T\right) - f\left(\frac{\omega_0}{2}, T\right) \right], \quad (6)$$

where  $\Gamma_0^{e-ph}$  is a residual damping rate, and  $f(\omega, T) = [e^{(\hbar\omega - E_F)/k_B T} + 1]^{-1}$  is the Fermi function. In this model, at higher temperatures, based on the Pauli exclusion principle, the thermally excited electrons and holes can suppress the electronic transitions at energy  $\hbar\omega_0$ , leading to less  $e$ - $ph$  scattering [45,52]. Consequently, the net damping rate is given by  $\Gamma(T) = \Gamma^{e-ph} + \Gamma^{\text{ph-ph}}$ . However, microscopically it is extremely difficult to derive an analytical expression to describe  $\omega_1(T)$  including both contributions. Nonetheless, we can assume that these two parameters phenomenologically follow a power-law-like ( $T^\alpha$ )  $T$ -dependent behavior, very similar to what has been done during discussion of the relaxation of another bosonic quasiparticle—spin [53]. Under such an assumption, we can fulfill the fit of experimental  $\omega_1$  and  $\Gamma_1$  in two separated temperature regimes divided by  $T^*$ ; i.e., for  $\omega_1$ , we use  $\omega^{\text{ph-ph}}(T)$  and power-law at  $T < T^*$  and  $T > T^*$ , respectively; and for  $\Gamma_1$ , we use  $\Gamma^{\text{ph-ph}}$  and  $\Gamma^{\text{ph-ph}} + \Gamma^{e-ph}$  at  $T < T^*$  and  $T > T^*$ , respectively. Figure 3(c) demonstrates that the fitted results agree very well with the experimental data and that they strongly support our interpretations. We note that the temperature dependence of the phonon mode  $\omega_1$  cannot be due to its interference with  $\omega_2$ , since no clear anomaly is observed at  $T = T^*$  in  $\omega_2(T)$  (see Fig. 8 in Appendix E).

### III. DISCUSSION

As mentioned above, the anomalous temperature-dependent behaviors of the recombination process characterized by  $\tau_2$  and the coherent optical phonon of the  $\omega_1$  mode should be associated with the sudden electronic structure change at  $T \sim T^*$ . Since no change of the crystal structure of NiTe<sub>2</sub> has been detected, our experiments suggest that the Lifshitz transition [25] potentially emerges in this material, i.e., an electronic

and topological transition defined by the change of Fermi surface topology without the symmetry breaking [26], which could be induced by the applied pressure [25,54], external magnetic field [55], temperature [1,2,56,57], and photoexcitation of ultrafast optical pulses [5]. In NiTe<sub>2</sub>, the pressure-induced Lifshitz transition has been proposed by observing anomalies of the pressure-dependent phonon spectrum and resistivity [25]. Therefore, we suspect that the unexpected variation of  $\tau_2(T)$  near  $T^*$  in our experiments may originate from the temperature-induced modification of the Fermi surface in  $k$ -space. As illustrated in Fig. 4(a), at  $T \geq T^*$ , more electron pockets might occur and hence open additional phonon-assisted  $e$ - $h$  recombination channels. As a result, there will appear sudden changes in the temperature-dependent carrier and coherent phonon dynamics that are engaged in. However, two requirements must be satisfied in this scenario: (i)  $E_F$  should be on the order of  $k_B T$  ( $< 100$  meV) [58]; (ii) Near  $E_F$  there exist intricate band structures with anomalous dispersion, which make abrupt change of the Fermi surface possible due to the shift of the chemical potential [56]. Evidently, these two conditions are satisfied in the NiTe<sub>2</sub> single crystal, where  $E_F$  is only  $\sim 20$ – $76$  meV lower than the Dirac point and cuts through the conduction band, the valance band, and the Dirac cone [18,20,40] [see Fig. 4(a)].

In fact, the temperature-dependent resistance also discloses an anomaly around 60 K [see Fig. 4(b)], which means the carrier or scattering properties near  $E_F$  undergo some changes. More strong evidence confirming the electronic transition in NiTe<sub>2</sub> can be revealed by the Hall measurement, which enables us to identify the carrier types at different temperatures. The measured  $\rho_{xy}$  as functions of the applied external magnetic field at temperatures from 20 to 200 K are shown in Fig. 4(c). Clearly, a sign flip of its slope appears at  $T \sim 60$  K and directly unveils the change of carrier types as a result of the populated states varying in the electron and hole pockets via the temperature-driven shift of the chemical potential [see Fig. 4(a)]. Such an observation establishes a sudden transformation around  $T^*$  in the temperature evolution of the Fermi surface.

Based on the discussions above, the exotic temperature dependence of carrier dynamics ( $\tau_2$ ) and coherent phonons ( $\omega_1$ ) could be understood well by considering the electronic

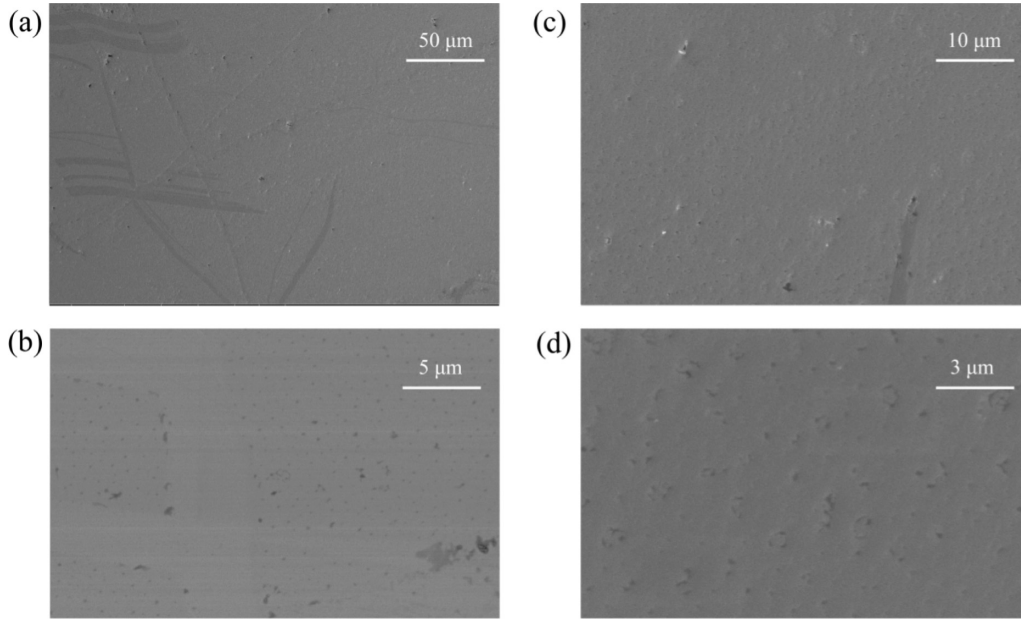


FIG. 5. The surface morphology of NiTe<sub>2</sub> from SEM measurement with different scales.

structure change around  $T^*$ , i.e., the Lifshitz transition. We note that the transition temperature  $T^*$  is only 60 K, whose corresponding energy ( $k_B T \sim 5.2$  meV) is much less than the Fermi energy ( $E_F \sim 20\text{--}76$  meV); such a transition should be mainly contributed to the topological nontrivial bands rather than the Dirac cone as shown in Fig. 4(a). Also, we note that because the electronic transition in this work is observed nearly at the same temperature in both the transport and the optical experiments, it should be due to the thermal-originated chemical potential shift rather than to the optical-induced band structure renormalization in our pump-probe experiments. Although we cannot fully exclude the latter one, its contribution should be very small due to the extremely low excitation fluence compared to the previous work in WTe<sub>2</sub>[5], where the optical-induced Lifshitz transition was observed with fluences of more than  $2$  mJ/cm<sup>2</sup>, which is almost larger by 3 orders of magnitude than those in our experiments.

Moreover, although our results reveal the influence of the Lifshitz transition on the ultrafast dynamics of the topological semimetal NiTe<sub>2</sub>, details of the Fermi surface change and the related momentum-dependent effects deserve further explorations in the future.

#### IV. SUMMARY

In conclusion, we have demonstrated that the ultrafast carrier and phonon dynamics in NiTe<sub>2</sub> can be tuned by the Lifshitz transition. The relaxation process ( $\tau_2$ ) of carriers and the amplitude and frequency of the coherent phonon ( $\omega_1$ ) show unexpected temperature dependence at  $T^*$  ( $\sim 60$  K), where the electronic transition emerges. The abrupt change of the electronic structure at  $T^*$  can mediate the carrier recombination and electron-phonon interaction and further affect the electromagnetic response of NiTe<sub>2</sub>. This proves the feasibility to manipulate the nonequilibrium carrier and lattice responses in a variety of material systems with similar electronic

structures. Also, our findings will benefit the development of future ultrafast electronic and optoelectronic devices based on the topological materials.

#### ACKNOWLEDGMENTS

This work was supported by the National Natural Science Foundation of China (Grants No. 11974070, No. 11734006, No. 11925408, No. 11921004, No. 12004067, No. 11904165, and No. 62027807), the Frontier Science Project of Dongguan (Grant No. 2019622101004), the CAS Interdisciplinary Innovation Team, and the Beijing National Laboratory for Condensed Matter Physics.

#### APPENDIX A: SAMPLE CHARACTERIZATION

The NiTe<sub>2</sub> sample was characterized by the energy dispersive spectrum (EDS), x-ray diffraction (XRD), and scanning electron microscopy (SEM), respectively.

The EDS and XRD results of our sample can be found in Ref. [21]. The EDS measurement clearly indicates the Ni and Te peaks with a perfect atomic ratio of 1:2, and XRD shows the single-crystal diffraction pattern without impurity peaks, indicating the high quality of the crystals. Figure 5 shows the morphology of NiTe<sub>2</sub> measured by SEM, and its relatively smooth and uniform surface ensures the good quality of the sample for optical measurements.

#### APPENDIX B: TWO-TEMPERATURE MODEL (TTM)

Based on the TTM, the electron-phonon energy relaxation time  $\tau$  is given by [34]

$$\tau = \frac{\gamma(T_e^2 - T_l^2)}{2H(T_e, T_l)}, \quad (\text{B1})$$

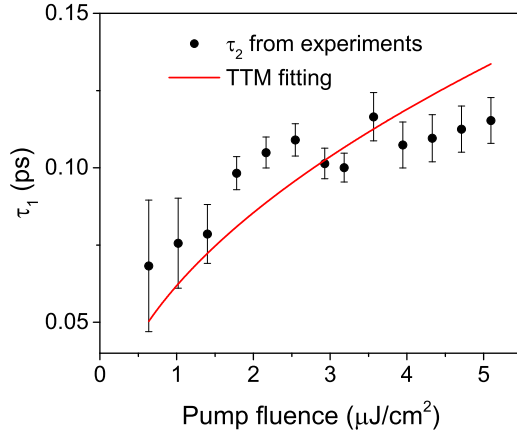


FIG. 6. The value of  $\tau_1$  as a function of pump fluence, and the curve represents the TTM fitting.

where  $\gamma$  is the electronic specific heat (Sommerfeld) coefficient, and the expression of  $H(T_e, T_l)$  is

$$H(T_e, T_l) = f(T_e) - f(T_l), \quad (\text{B2})$$

$$f(T) = 4g_\infty \frac{T^5}{\theta_D^4} \int_0^{\theta_D/T} \frac{x^4}{e^x - 1} dx, \quad (\text{B3})$$

where  $T_e$  and  $T_l$  are temperatures of electron and lattice subsystems, respectively, and  $g_\infty$  is the electron-phonon coupling constant. The temperature of electrons can be estimated by

$$T_e = \sqrt{T_l^2 + \frac{2U_l}{\gamma}}, \quad (\text{B4})$$

where  $U_l$  is energy density of laser light, which can be calculated according to the experimental conditions. The fitting of  $\tau_1$  (the fast relaxation process mentioned in the main text) as a function of temperature in the TTM is shown as a solid line in Fig. 2(a) in the main text.

### APPENDIX C: FLUENCE DEPENDENCE OF $\tau_1$

$\tau_1$  as a function of pump fluence is shown in Fig. 6, which is obtained from  $\Delta R/R$  measured at 80 K. The curve in Fig. 6 is from the TTM fitting as mentioned in Appendix A. The good fitting quality is consistent with the  $T$ -dependent fitting as shown in Fig. 2(a), suggesting that the TTM is appropriate to describe the fast relaxation process in our observations.

### APPENDIX D: POLARIZATION DEPENDENCE OF PHONON MODES

We also performed the pump-polarization-dependent experiments on NiTe<sub>2</sub>, and the amplitudes of the oscillations (in frequency domain) are shown in Fig. 7. It is obvious that there are three phonon peaks, and only the  $E_g$  mode ( $\omega_3$ ) is dependent on the pump polarization. Therefore, in the study of coherent phonons, we choose the pump polarization angle

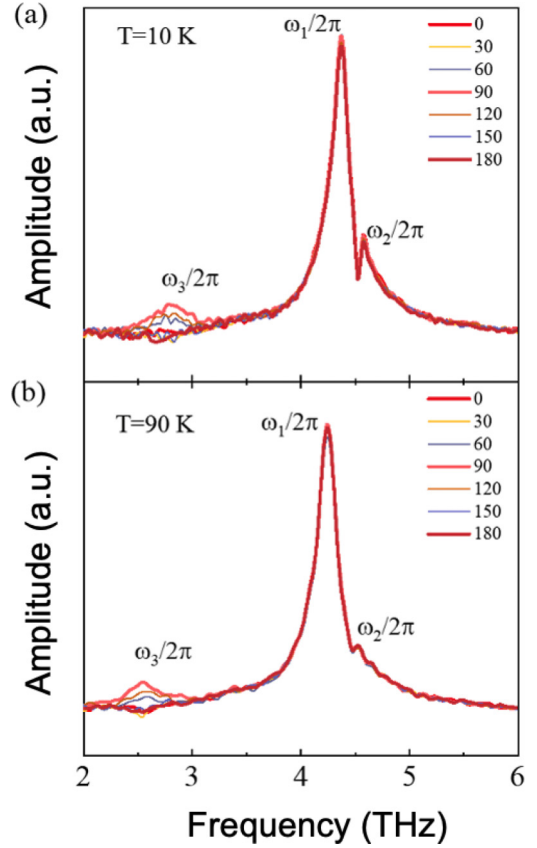


FIG. 7. FFT amplitudes of oscillations with different pump polarization angles, at 10 and 90 K.

as  $0^\circ$  to minimize the contributions of the  $\omega_3$  phonon, which can simplify the data analysis process.

### APPENDIX E: EXTRACTED PARAMETERS OF PHONON MODE $\omega_2$

The extracted frequency of  $\omega_2$  as a function of temperature are shown in Fig. 8. We can see that the uncertainties of  $\omega_2$  are large at high temperatures due to the amplitude

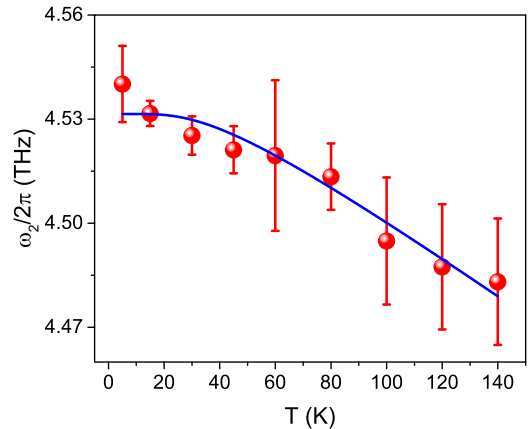


FIG. 8. The extracted frequency of the mode  $\omega_2$ . The blue curve represents the anharmonic phonon model fitting.

of this mode diminishing quickly with increasing  $T$ . However, we can still fit the data with the anharmonic phonon model, and the result shows acceptable fitting quality,

which also indicates that the temperature-dependent behavior of  $\omega_2$  could be explained by the anharmonic phonon model.

- 
- [1] Y. Zhang, C. Wang, L. Yu, G. Liu, A. Liang, J. Huang, S. Nie, X. Sun, Y. Zhang, B. Shen, J. Liu, H. Weng, L. Zhao, G. Chen, X. Jia, C. Hu, Y. Ding, W. Zhao, Q. Gao, C. Li *et al.*, Electronic evidence of temperature-induced Lifshitz transition and topological nature in  $\text{ZrTe}_5$ , *Nat. Commun.* **8**, 15512 (2017).
- [2] Y. Wu, N. H. Jo, M. Ochi, L. Huang, D. Mou, S. L. Bud'ko, P. C. Canfield, N. Trivedi, R. Arita, and A. Kaminski, Temperature-Induced Lifshitz Transition in  $\text{WTe}_2$ , *Phys. Rev. Lett.* **115**, 166602 (2015).
- [3] C. Liu, T. Kondo, R. M. Fernandes, A. D. Palczewski, E. D. Mun, N. Ni, A. N. Thaler, A. Bostwick, E. Rotenberg, J. Schmalian, S. L. Bud'ko, P. C. Canfield, and A. Kaminski, Evidence for a Lifshitz transition in electron-doped iron arsenic superconductors at the onset of superconductivity, *Nat. Phys.* **6**, 419 (2010).
- [4] G. E. Volovik, Exotic Lifshitz transitions in topological materials, *Phys.-Usp.* **61**, 89 (2018).
- [5] S. Beaulieu, S. Dong, N. Tancogne-Dejean, M. Dendzik, T. Pincelli, J. Maklar, R. P. Xian, M. A. Sentef, M. Wolf, A. Rubio, L. Rettig, and R. Ernstorfer, Ultrafast dynamical Lifshitz transition, *Sci. Adv.* **7**, eabd9275 (2021).
- [6] M. G. Hell, N. Ehlen, B. V. Senkovskiy, E. H. Hasdeo, A. Fedorov, D. Dombrowski, C. Busse, T. Michely, G. di Santo, L. Petaccia, R. Saito, and A. Grüneis, Resonance Raman spectrum of doped epitaxial graphene at the Lifshitz transition, *Nano Lett.* **18**, 6045 (2018).
- [7] T. Biesner, W. Li, A. A. Tsirlin, S. Roh, P.-C. Wei, E. Uykur, and M. Dressel, Spectroscopic trace of the Lifshitz transition and multivalley activation in thermoelectric  $\text{SnSe}$  under high pressure, *NPG Asia Mater.* **12**, 1884 (2021).
- [8] A. A. Burkov, Topological semimetals, *Nat. Mater.* **15**, 1145 (2016).
- [9] H. Weng, X. Dai, and Z. Fang, Topological semimetals predicted from first-principles calculations, *J. Phys.: Condens. Matter* **28**, 303001 (2016).
- [10] B. Yan and C. Felser, Topological materials: Weyl semimetals, *Annu. Rev. Condens. Matter Phys.* **8**, 337 (2017).
- [11] N. P. Armitage, E. J. Mele, and A. Vishwanath, Weyl and Dirac semimetals in three-dimensional solids, *Rev. Mod. Phys.* **90**, 015001 (2018).
- [12] A. A. Soluyanov, D. Gresch, Z. Wang, Q. Wu, M. Troyer, X. Dai, and B. A. Bernevig, Type-II Weyl semimetals, *Nature (London)* **527**, 495 (2015).
- [13] Z. Wang, D. Gresch, A. A. Soluyanov, W. Xie, S. Kushwaha, X. Dai, M. Troyer, R. J. Cava, and B. A. Bernevig,  $\text{MoTe}_2$ : A Type-II Weyl Topological Metal, *Phys. Rev. Lett.* **117**, 056805 (2016).
- [14] Y.-Y. Lv, X. Li, B.-B. Zhang, W. Y. Deng, S.-H. Yao, Y. B. Chen, J. Zhou, S.-T. Zhang, M.-H. Lu, L. Zhang, M. Tian, L. Sheng, and Y.-F. Chen, Experimental Observation of Anisotropic Adler-Bell-Jackiw Anomaly in Type-II Weyl Semimetal  $\text{WTe}_{1.98}$  Crystals at the Quasiclassical Regime, *Phys. Rev. Lett.* **118**, 096603 (2017).
- [15] M. Udagawa and E. J. Bergholtz, Field-Selective Anomaly and Chiral Mode Reversal in Type-II Weyl Materials, *Phys. Rev. Lett.* **117**, 086401 (2016).
- [16] M. Alidoust, K. Halterman, and A. A. Zyuzin, Superconductivity in type-II Weyl semimetals, *Phys. Rev. B* **95**, 155124 (2017).
- [17] T. E. O'Brien, M. Diez, and C. W. J. Beenakker, Magnetic Breakdown and Klein Tunneling in a Type-II Weyl Semimetal, *Phys. Rev. Lett.* **116**, 236401 (2016).
- [18] C. Xu, B. Li, W. Jiao, W. Zhou, B. Qian, R. Sankar, N. D. Zhigadlo, Y. Qi, D. Qian, F.-C. Chou, and X. Xu, Topological type-II Dirac fermions approaching the Fermi level in a transition metal dichalcogenide  $\text{NiTe}_2$ , *Chem. Mater.* **30**, 4823 (2018).
- [19] J. Zhang and G. Q. Huang, The superconductivity and topological surface state of type-II Dirac semimetal  $\text{NiTe}_2$ , *J. Phys.: Condens. Matter* **32**, 205702 (2020).
- [20] B. Ghosh, D. Mondal, C.-N. Kuo, C. S. Lue, J. Nayak, J. Fujii, I. Vobornik, A. Politano, and A. Agarwal, Observation of bulk states and spin-polarized topological surface states in transition metal dichalcogenide Dirac semimetal candidate  $\text{NiTe}_2$ , *Phys. Rev. B* **100**, 195134 (2019).
- [21] Q. Liu, F. Fei, B. Chen, X. Bo, B. Wei, S. Zhang, M. Zhang, F. Xie, M. Naveed, X. Wan, F. Song, and B. Wang, Nontopological origin of the planar Hall effect in the type-II Dirac semimetal  $\text{NiTe}_2$ , *Phys. Rev. B* **99**, 155119 (2019).
- [22] J. Shi, Y. Huan, M. Xiao, M. Hong, X. Zhao, Y. Gao, F. Cui, P. Yang, S. J. Pennycook, J. Zhao, and Y. Zhang, Two-dimensional metallic  $\text{NiTe}_2$  with ultrahigh environmental stability, conductivity, and electrocatalytic activity, *ACS Nano* **14**, 9011 (2020).
- [23] W. Zheng, R. Schönemann, S. Mozaffari, Y.-C. Chiu, Z. B. Goraum, N. Aryal, E. Manousakis, T. M. Siegrist, K. Wei, and L. Balicas, Bulk Fermi surfaces of the dirac type-II semimetallic candidate  $\text{NiTe}_2$ , *Phys. Rev. B* **102**, 125103 (2020).
- [24] S. Nappini, D. W. Boukhvalov, G. D'Olimpio, L. Zhang, B. Ghosh, C.-N. Kuo, H. Zhu, J. Cheng, M. Nardone, L. Ottaviano, D. Mondal, R. Edla, J. Fuji, C. S. Lue, I. Vobornik, J. A. Yarmoff, A. Agarwal, L. Wang, L. Zhang, F. Bondino *et al.*, Transition-metal dichalcogenide  $\text{NiTe}_2$ : An ambient-stable material for catalysis and nanoelectronics, *Adv. Funct. Mater.* **30**, 2000915 (2020).
- [25] M. Qi, C. An, Y. Zhou, H. Wu, B. Zhang, C. Chen, Y. Yuan, S. Wang, Y. Zhou, X. Chen, R. Zhang, and Z. Yang, Pressure-driven Lifshitz transition in type-II Dirac semimetal  $\text{NiTe}_2$ , *Phys. Rev. B* **101**, 115124 (2020).
- [26] I. M. Lifshitz, Anomalies of electron characteristics of a metal in the high pressure region, *Journal of Experimental and Theoretical Physics* **11**, 1130 (1960).
- [27] J. Qi, T. Durakiewicz, S. A. Trugman, J.-X. Zhu, P. S. Riseborough, R. Baumbach, E. D. Bauer, K. Gofryk, J.-Q. Meng, J. J. Joyce, A. J. Taylor, and R. P. Prasankumar, Measurement of Two Low-Temperature Energy Gaps in the Electronic



- Structure of Antiferromagnetic  $\text{USB}_2$  Using Ultrafast Optical Spectroscopy, *Phys. Rev. Lett.* **111**, 057402 (2013).
- [28] M. C. Wang, S. Qiao, Z. Jiang, S. N. Luo, and J. Qi, Unraveling Photoinduced Spin Dynamics in the Topological Insulator  $\text{Bi}_2\text{Se}_3$ , *Phys. Rev. Lett.* **116**, 036601 (2016).
- [29] M. C. Wang, H. S. Yu, J. Xiong, Y.-F. Yang, S. N. Luo, K. Jin, and J. Qi, Bosonic excitations and electron pairing in an electron-doped cuprate superconductor, *Phys. Rev. B* **97**, 155157 (2018).
- [30] Y. P. Liu, Y. J. Zhang, J. J. Dong, H. Lee, Z. X. Wei, W. L. Zhang, C. Y. Chen, H. Q. Yuan, Y.-f. Yang, and J. Qi, Hybridization Dynamics in  $\text{CeCoIn}_5$  Revealed by Ultrafast Optical Spectroscopy, *Phys. Rev. Lett.* **124**, 057404 (2020).
- [31] D. J. Hilton and C. L. Tang, Optical Orientation and Femtosecond Relaxation of Spin-Polarized Holes in GaAs, *Phys. Rev. Lett.* **89**, 146601 (2002).
- [32] L. Cheng, C. La-o-vorakiat, C. S. Tang, S. K. Nair, B. Xia, L. Wang, J.-X. Zhu, and E. E. M. Chia, Temperature-dependent ultrafast carrier and phonon dynamics of topological insulator  $\text{Bi}_{1.5}\text{Sb}_{0.5}\text{Te}_{1.8}\text{Se}_{1.2}$ , *Appl. Phys. Lett.* **104**, 211906 (2014).
- [33] P. B. Allen, Theory of Thermal Relaxation of Electrons in Metals, *Phys. Rev. Lett.* **59**, 1460 (1987).
- [34] R. H. M. Groeneveld, R. Sprik, and A. Lagendijk, Femtosecond spectroscopy of electron-electron and electron-phonon energy relaxation in Ag and Au, *Phys. Rev. B* **51**, 11433 (1995).
- [35] J. Demsar, R. D. Averitt, K. H. Ahn, M. J. Graf, S. A. Trugman, V. V. Kabanov, J. L. Sarrao, and A. J. Taylor, Quasiparticle Relaxation Dynamics in Heavy Fermion Compounds, *Phys. Rev. Lett.* **91**, 027401 (2003).
- [36] M. Hase, K. Ishioka, J. Demsar, K. Ushida, and M. Kitajima, Ultrafast dynamics of coherent optical phonons and nonequilibrium electrons in transition metals, *Phys. Rev. B* **71**, 184301 (2005).
- [37] R. C. Hatch, M. Bianchi, D. Guan, S. Bao, J. Mi, B. B. Iversen, L. Nilsson, L. Hornekær, and P. Hofmann, Stability of the  $\text{Bi}_2\text{Se}_3(111)$  topological state: Electron-phonon and electron-defect scattering, *Phys. Rev. B* **83**, 241303(R) (2011).
- [38] D. Niesner, S. Otto, V. Hermann, T. Fauster, T. V. Menshchikova, S. V. Eremeev, Z. S. Aliev, I. R. Amiraslanov, M. B. Babanly, P. M. Echenique, and E. V. Chulkov, Bulk and surface electron dynamics in a  $p$ -type topological insulator  $\text{SnSb}_2\text{Te}_4$ , *Phys. Rev. B* **89**, 081404(R) (2014).
- [39] A. Othonos, Probing ultrafast carrier and phonon dynamics in semiconductors, *J. Appl. Phys.* **83**, 1789 (1998).
- [40] S. Mukherjee, S. W. Jung, S. F. Weber, C. Xu, D. Qian, X. Xu, P. K. Biswas, T. K. Kim, L. C. Chapon, M. D. Watson, J. B. Neaton, and C. Cacho, Fermi-crossing type-II Dirac fermions and topological surface states in  $\text{NiTe}_2$ , *Sci. Rep.* **10**, 12957 (2020).
- [41] M. Rasolt, Plasmon-phonon-assisted electron-hole recombination in Si at very high carrier density, *Phys. Rev. B* **33**, 1166 (1986).
- [42] A. A. Lopez, Electron-hole recombination in bismuth, *Phys. Rev.* **175**, 823 (1968).
- [43] Y. M. Sheu, Y. J. Chien, C. Uher, S. Fahy, and D. A. Reis, Free-carrier relaxation and lattice heating in photoexcited bismuth, *Phys. Rev. B* **87**, 075429 (2013).
- [44] Y. M. Dai, J. Bownan, H. Li, H. Miao, S. F. Wu, W. D. Kong, P. Richard, Y. G. Shi, S. A. Trugman, J.-X. Zhu, H. Ding, A. J. Taylor, D. A. Yarotski, and R. P. Prasankumar, Ultrafast carrier dynamics in the large-magnetoresistance material  $\text{WTe}_2$ , *Phys. Rev. B* **92**, 161104(R) (2015).
- [45] B. Xu, Y. M. Dai, L. X. Zhao, K. Wang, R. Yang, W. Zhang, J. Y. Liu, H. Xiao, G. F. Chen, S. A. Trugman, J.-X. Zhu, A. J. Taylor, D. A. Yarotski, R. P. Prasankumar, and X. G. Qiu, Temperature-tunable Fano resonance induced by strong coupling between Weyl fermions and phonons in TaAs, *Nat. Commun.* **8**, 14933 (2017).
- [46] G. A. Garrett, T. F. Albrecht, J. F. Whitaker, and R. Merlin, Coherent THz Phonons Driven by Light Pulses and the Sb Problem: What is the Mechanism? *Phys. Rev. Lett.* **77**, 3661 (1996).
- [47] R. Merlin, Generating coherent THz phonons with light pulses, *Solid State Commun.* **102**, 207 (1997).
- [48] J. Menéndez and M. Cardona, Temperature dependence of the first-order Raman scattering by phonons in Si, Ge, and  $\alpha$ -Sn: Anharmonic effects, *Phys. Rev. B* **29**, 2051 (1984).
- [49] T. R. Hart, R. L. Aggarwal, and B. Lax, Temperature dependence of Raman scattering in silicon, *Phys. Rev. B* **1**, 638 (1970).
- [50] M. Balkanski, R. F. Wallis, and E. Haro, Anharmonic effects in light scattering due to optical phonons in silicon, *Phys. Rev. B* **28**, 1928 (1983).
- [51] K. Watanabe, N. Takagi, and Y. Matsumoto, Direct Time-Domain Observation of Ultrafast Dephasing in Adsorbate-Substrate Vibration under the Influence of a Hot Electron Bath: Cs Adatoms on Pt(111), *Phys. Rev. Lett.* **92**, 057401 (2004).
- [52] N. Bonini, M. Lazzeri, N. Marzari, and F. Mauri, Phonon Anharmonicities in Graphite and Graphene, *Phys. Rev. Lett.* **99**, 176802 (2007).
- [53] I. Žutić, J. Fabian, and S. Das Sarma, Spintronics: Fundamentals and applications, *Rev. Mod. Phys.* **76**, 323 (2004).
- [54] H. F. Yang, L. X. Yang, Z. K. Liu, Y. Sun, C. Chen, H. Peng, M. Schmidt, D. Prabhakaran, B. A. Bernevig, C. Felser, B. H. Yan, and Y. L. Chen, Topological Lifshitz transitions and Fermi arc manipulation in Weyl semimetal NbAs, *Nat. Commun.* **10**, 3478 (2019).
- [55] H. Pfau, R. Daou, S. Lausberg, H. R. Naren, M. Brando, S. Friedemann, S. Wirth, T. Westerkamp, U. Stockert, P. Gegenwart, C. Krellner, C. Geibel, G. Zwirgagl, and F. Steglich, Interplay between Kondo Suppression and Lifshitz Transitions in  $\text{YbRh}_2\text{Si}_2$  at High Magnetic Fields, *Phys. Rev. Lett.* **110**, 256403 (2013).
- [56] A. I. Coldea, S. F. Blake, S. Kasahara, A. A. Haghighirad, M. D. Watson, W. Knafo, E. S. Choi, A. McCollam, P. Reiss, T. Yamashita, M. Bruma, S. C. Speller, Y. Matsuda, T. Wolf, T. Shibauchi, and A. J. Schofield, Evolution of the low-temperature Fermi surface of superconducting  $\text{FeSe}_{1-x}\text{S}_x$  across a nematic phase transition, *npj Quantum Mater.* **4**, 2 (2019).
- [57] S. Y. Back, Y.-K. Kim, H. Cho, M.-K. Han, S.-J. Kim, and J. S. Rhyee, Temperature-induced Lifshitz transition and charge density wave in  $\text{InTe}_{1-\delta}$  thermoelectric materials, *ACS Appl. Energy Mater.* **3**, 3628 (2020).
- [58] J. Wang, H. Yang, L. Ding, W. You, C. Xi, J. Cheng, Z. Shi, C. Cao, Y. Luo, Z. Zhu, J. Dai, M. Tian, and Y. Li, Angle-dependent magnetoresistance and its implications for Lifshitz transition in  $\text{W}_2\text{As}_3$ , *npj Quantum Mater.* **4**, 58 (2019).